Available online at www.sciencedirect.com
ScienceDirect
Journal of Sound and Vibration 315 (2008) 433–454
JOURNAL OF SOUND AND VIBRATION
www.elsevier.com/locate/jsvi

Numerical simulation of the dynamic responses of railway overhead contact lines to a moving pantograph, considering a nonlinear dropper

Yong Hyeon Cho*

Korea Railroad Research Institute (KRRI), 360-1, Woram-dong Uiwang-city, Gyeonggi-do 437-757, Republic of Korea

Received 12 February 2008; accepted 13 February 2008
The peer review of this article was organised by the Guest Editor
Available online 18 April 2008

Abstract

Both the formulation of a nonlinear dropper and the proper implementation of a time-integration method are proposed for the finite element method (FEM) of pantograph–overhead contact line dynamics. The FEM models for a pantograph, overhead contact lines and dynamic interaction between a pantograph and overhead contact lines are validated step by step, by comparing simulated results with measured results. The dynamic responses of overhead contact lines to a moving pantograph, relevant to geometrically nonlinear droppers, are presented.

1. Introduction

Railway overhead contact lines consist of a contact wire, a messenger wire, droppers, supporting brackets, and registration arms, as shown in Fig. 1. The contact wire and the messenger wire are connected by the periodically placed droppers. The messenger wire is supported by the supporting brackets. The registration arms are installed to the contact wire. Stagger is required for even wear of the contact strip of a pantograph. The pantograph on the roof of an electric train receives current from the contact wire through the contact between the contact wire and the pantograph. Improved current collection performance is one of the key requirements for railway speed-up, which is an issue of great importance in the railway industry.

Many studies have examined the response of the pantograph–overhead contact lines. Under the assumption that the overhead contact lines are represented by a tensioned string supported by an elastic medium whose stiffness periodically varies with location, the motion of the string was analytically described [1]. In consideration of wave propagation in a string, the interaction between the pantograph and the reflected wave was mathematically investigated [2]. An overview of the simulation methods available for the pantograph–overhead contact line dynamics was presented [3]. The dynamic stiffness of the overhead contact lines depending on both speed of movement and wave propagation speed in the contact wire was investigated

*Tel.: +82 31 460 5112; fax: +82 31 460 5459.
E-mail address: yhcho@krri.re.kr

0022-460X/$ - see front matter © 2008 Elsevier Ltd. All rights reserved.
doi:10.1016/j.jsv.2008.02.024

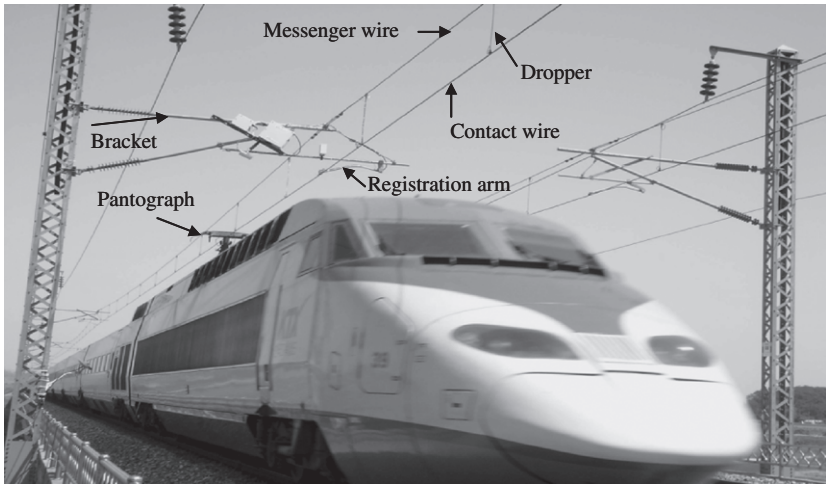

Fig. 1. A simple catenary type of railway overhead contact lines.

[4]. The steady-state response of two-level overhead contact lines to a moving pantograph was analyzed by using the Fourier transformation and the periodicity condition [5]. For the purpose of sensitivity analysis for the pantograph, numerical analyses used a simplified overhead contact line model together with a linear lumped model of the pantograph [6,7]. The improvement to the simplified numerical analysis incorporated the influence of the stiffness and the contact modeling [8]. Based on previous studies, the variation of the contact force between the pantograph and the contact wire is mainly caused by both the stiffness variation along the span and the wave reflection. Because the simplified railway overhead contact line model considers only the stiffness variation along a span, it does not allow wave propagation in a contact wire. Thus, simplified numerical analyses insufficiently evaluate the variation of the contact force in the high-speed range, where the wave reflection becomes a major cause for the loss of contact. In order to describe more accurately the dynamic interaction between a pantograph and overhead contact lines, full numerical simulations accounting for the effect of wave reflection on the contact force should be performed. The finite element method (FEM) is currently used in most simulation studies because the geometry of the overhead contact lines is complicated [9–12]. In this study, a spatial finite element approach is combined with a numerical time-integration method to analyze the response of railway overhead contact lines to a moving pantograph.

The aims of this paper are to propose the formulation of a nonlinear dropper in overhead contact lines, to study the proper implementation of numerical time-integration associated with wave propagation and to discuss validation of the finite element analysis of pantograph–overhead contact line dynamics by using measurements in the field.

The slackening of droppers is taken into account as a unique source of geometrical nonlinearities, that is, the dropper has no resistance to the motion if it becomes slack in compression. Because the slackening of the droppers significantly influences the response of the railway overhead contact lines due to a moving pantograph, the formulation of a nonlinear dropper has been previously studied. For the dynamic simulation in Ref. [10], the droppers were replaced with external forces applied to the contact wire and the messenger wire. The external forces were determined by interpolations of the dropper's force versus deformation characteristics, based on the deformation of the droppers at the previous time step. However, it is difficult to represent the slackening of the droppers explicitly when dissipative effects in the droppers are important. In Ref. [11], joint constraints between the contact wire and the messenger wire were analyzed using Lagrange multipliers. The corresponding Lagrange multipliers were monitored to determine the slackening of the droppers. According to Refs. [13,14], the bending strain in a contact wire near the dropper is always a compressive type of strain. When the pantograph is under the dropper, the strain instantaneously becomes tensile. Afterward, it immediately returns to being compressive strain. However, in Ref. [11], the dynamic

strain at the dropper location was always tensile when the pantograph passed the dropper. Thus, an improved formulation for the nonlinear dropper is needed. In previous studies, the formulation of a nonlinear dropper was not validated. Here, I propose to validate the formulation of a nonlinear dropper, one which accurately represents the slackening of the real droppers, by comparing the simulated internal forces on the dropper with those forces measured when the pantograph passes the dropper in the field.

Secondly, I study the proper implementation of a numerical time-integration method associated with wave propagation in a tensioned beam. The dynamic interaction between a pantograph and a contact wire constitutes a typical wave propagation problem. Wave propagation speed in a contact wire increases as the excitation frequency increases. According to EN 50119:2001 [15], contact forces between a pantograph and a contact wire shall be simulated for every 0.2 m of the contact wire in order to evaluate current collection quality. If it is assumed that a train moves at 200 km h^{-1}, the 0.2 m corresponds to a time step of 0.0036 s. It is necessary to check whether a time step as long as 0.003 s for numerical time-integration is valid in order to represent the wave propagation in a contact wire. However, the correct time step for pantograph–overhead line simulations has not been discussed in previous studies, and so I discuss it here. The reduction of spurious oscillations should also be taken into account to obtain the accurate characteristics of wave reflection. In Ref. [10], spurious oscillations were reduced by increasing the order of the shape function for the beam elements or by refining the finite element mesh. Spurious oscillations can also be reduced by the numerical damping of numerical time-integration [20]. Thus, in this study, I investigate the necessity of numerical damping for the pantograph–overhead contact line dynamics by solving a "wave propagation in a pre-tensioned beam" problem.

Thirdly, I discuss the validation of the pantograph–overhead contact line dynamic simulations by using measurements in the field. It is important to verify that an overhead contact line model has wave propagation characteristics similar to the real overhead contact lines. There has been little discussion on the validation of the overhead contact line model. Thus, I validate the overhead contact line model by using an experimental result related to the wave reflection by periodically installed droppers. In Refs. [10–12], simulated vertical displacements of the contact wire and/or simulated contact forces between a pantograph and a contact wire were compared with measurements for the validation of the pantograph–overhead contact line simulations. However, the contact forces were not directly measured values, but estimated values from the pan-head accelerations and the spring-reaction forces exerted on the pan-head. For a more thorough validation, I perform the validation by using other direct measurements. Recently, the simulation of dynamic strains in a contact wire has been studied [11,16], but the simulated strains were not validated by measurements taken when a pantograph passes. Compared with vertical displacements, the higher eigenmodes in a contact wire play an important role in simulating dynamic strains in a contact wire [17], and so the validation by dynamic strains is more difficult than that by vertical displacements. Thus, I compare simulated dynamic strains in a contact wire with the directly measured strains for the validation in this study.

After validating the formulation, I discuss the dynamic responses of overhead contact lines due to a moving pantograph relevant to the geometrically nonlinear dropper.

This paper is organized in the following manner. Section 2 describes the finite element formulation, including both the nonlinear dropper and the time-integration method. Section 3 provides four FEM model validations. The first is for the pantograph model. The second is for the nonlinear dropper model to represent the slackening of the dropper. The third is for the overhead contact line model. The fourth is for the dynamic interaction between the pantograph and the contact wire. Section 4 deals with the dynamic responses of overhead contact lines due to a moving pantograph, relevant to the geometrically nonlinear dropper. Finally, Section 5 presents the main conclusion.

2. The formulation of the FEM

Because displacements in the lateral direction are negligible, I consider only vertical displacements for both the pantograph and the overhead contact lines. Dynamic simulation models for a pantograph and overhead contact lines are shown in Fig. 2.

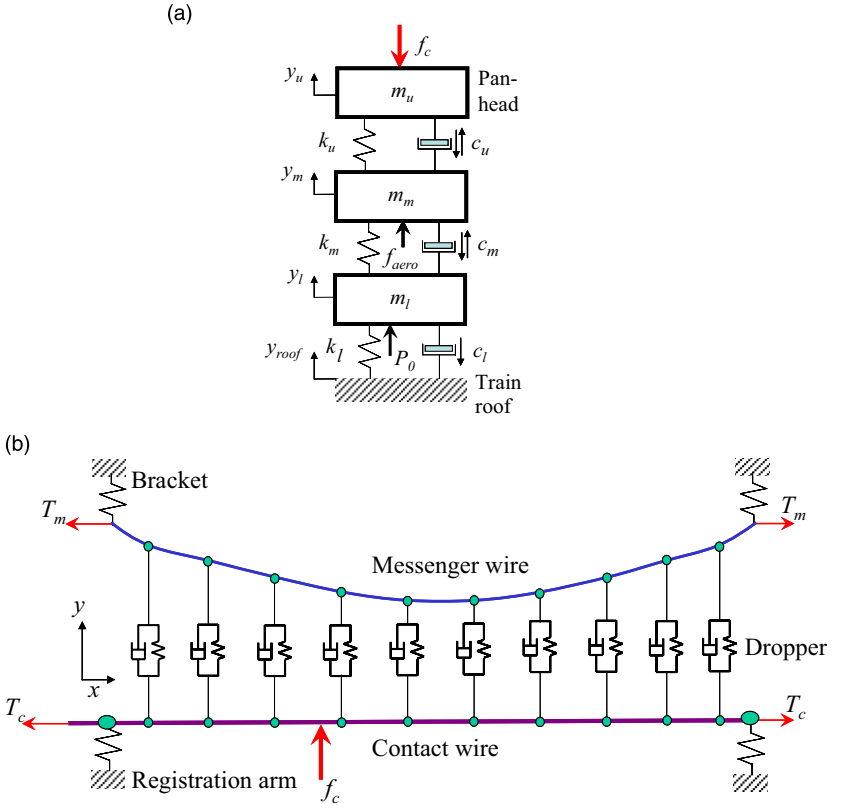

Fig. 2. Dynamic simulation model for the pantograph and the overhead contact lines: (a) a model of the Korean tilting pantograph and (b) a model of the overhead contact lines. ⬭ represents the mass of the registration arm. ● represents the mass summed for half of the dropper and its clamp.

2.1. Formulation for a pantograph

A pantograph can be modeled as two or three levels of the mass–spring–damper if the low-frequency motion of a pantograph is of interest. The pantograph in this study is the single-arm Korean tilting pantograph. A single-arm pantograph can be modeled as three levels of the mass–spring–damper, as shown in Fig. 2(a). The dynamic equation for the lumped pantograph model can be derived from Fig. 2(a) as

$$m_u\ddot{y}_u + c_u\dot{y}_u - c_u\dot{y}_m + k_u y_u - k_u y_m = -f_c \tag{1}$$

$$m_m\ddot{y}_m - c_m\dot{y}_l + (c_u + c_m)\dot{y}_m - c_u\dot{y}_u - k_m y_l + (k_u + k_m)y_m - k_u y_u = f_{\text{aero}} \tag{2}$$

$$m_l\ddot{y}_l + (c_l + c_m)\dot{y}_l - c_m\dot{y}_m + (k_l + k_m)y_l - k_m y_m = P_0 + c_l\dot{y}_{\text{roof}} + k_l y_{\text{roof}} \tag{3}$$

where y_u is the vertical displacement of the pan-head (m), y_m is the vertical displacement of the upper frame (m), y_l is the vertical displacement of the lower frame (m), y_{roof} is the vertical displacement of the train roof (m) and f_c is the contact force between a pantograph and a contact wire (N). The dot represents the derivative with respect to time. The definition of the other parameters in the above equations is given in Table 1. The damper between the lower arm and the train roof, c_l, is a nonlinear one-way damper to obtain better current collection. The one-way damper has a high damping value for a downward motion and a low damping value for an upward motion.

Table 1
Definition of parameters for the pantograph simulation model

Parameter	Definition
m_u	Mass of the pan-head
m_m	Mass of the upper frame
m_l	Mass of the lower frame
c_u	Damping coefficient between the pan-head and the upper frame
c_m	Damping coefficient between the upper frame and the lower frame
c_l	Damping coefficient between the lower frame and the train roof
P_0	Static uplift force
f_{aero}	Aerodynamic force
k_u	Stiffness coefficient between the pan-head and the upper frame
k_m	Stiffness coefficient between the upper frame and the lower frame
k_l	Stiffness coefficient between the lower frame and the train roof

2.2. Formulation for overhead contact lines

Assuming that the slope of a contact wire remains small, and that the tension applied to a contact wire is constant, the equation of motion for a contact wire (CW) can be derived from Fig. 2(b) as

$$\rho_c \frac{\partial^2 v_c(x,t)}{\partial t^2} + c_c(x,t)\frac{\partial v_c(x,t)}{\partial t} + \frac{\partial^2}{\partial x^2}\left(\mathrm{EI}_c \frac{\partial v_c^2(x,t)}{\partial x^2}\right) - T_c \frac{\partial^2 v_c(x,t)}{\partial x^2} + \sum_{i=1}^{\text{ndrop}} f_{\text{dr},i}(t)\delta(x-x_i) + \sum_{j=1}^{\text{nreg}} f_{\text{re},j}(t)\delta(x-x_j) - f_c(t)\delta(x-Vt) = 0 \tag{4}$$

where subscript c represents a contact wire, v_c represents vertical displacement from the equilibrium profile (m), ρ_c represents a line density ($\mathrm{kg\,m^{-1}}$), c_c represents a damping value ($\mathrm{N\,s\,m^{-1}}$), EI_c represents flexural rigidity ($\mathrm{N\,m^2}$), T_c represents tension (N), $f_c(t)$ represents a contact force (N), $\delta(x)$ represents a Dirac delta function at $x=0$, f_{dr} represents an external force by a dropper (N), ndrop represents the number of droppers, x_i represents the location of ith dropper (m), f_{re} represents an external force by a registration arm (N), nreg represents the number of registration arms, x_j represents the location of jth registration arm (m), V represents train speed ($\mathrm{m\,s^{-1}}$) and t represents time (s).

Under the assumption that the slope of a messenger wire is a small quantity, and that a tension applied to a messenger wire is constant, the equation of motion for a messenger wire (MW) can be derived from Fig. 2(b) as

$$\rho_m \frac{\partial^2 v_m(x,t)}{\partial t^2} + c_m(x,t)\frac{\partial v_m(x,t)}{\partial t} + \frac{\partial^2}{\partial x^2}\left(\mathrm{EI}_m \frac{\partial v_m^2(x,t)}{\partial x^2}\right) - T_m \frac{\partial^2 v_m(x,t)}{\partial x^2} - \sum_{i=1}^{\text{ndrop}} f_{\text{dr},i}(t)\delta(x-x_i) + \sum_{k=1}^{\text{nbrk}} f_{\text{br},k}(t)\delta(x-x_k) = 0 \tag{5}$$

where subscript m denotes a messenger wire, v_m denotes a vertical displacement from the equilibrium profile (m), ρ_m denotes a line density ($\mathrm{kg\,m^{-1}}$), c_m denotes a damping value ($\mathrm{N\,s\,m^{-1}}$), EI_m represents flexural rigidity ($\mathrm{N\,m^2}$), T_m denotes a tension (N), f_{br} denotes an external force by a bracket (ii), nbrk denotes the number of brackets, and x_k denotes the location of kth bracket (m).

A contact wire and a messenger wire are modeled using the 2-node Euler–Bernoulli beam element. For the calculation of a stiffness matrix, pre-tension and flexural rigidity are taken into account for both the contact wire and the messenger wire. While both registration arms and brackets are modeled using a mass–spring, a dropper is modeled using a mass–spring–damper, as shown in Fig. 2(b). The overhead contact lines in this

Table 2
Parameters of the Korean Honam overhead contact lines

Parameter	Value	Parameter	Value
Contact wire tension, T_c	12 kN	Messenger wire tension, T_m	12 kN
Contact wire density, ρ_c	0.987 kg m^{-1}	Messenger wire density, ρ_m	0.605 kg m^{-1}
Contact wire flexural rigidity, EI_c	130 N m^2	Messenger wire flexural rigidity, EI_m	29 N m^2
Dropper stiffness, k_d	1×10^5 N m^{-1}	Dropper damping value, c_d	5 N s m^{-1}
Registration arm stiffness on CW, k_r	213 N m^{-1}	Bracket stiffness on MW, k_b	2×10^6 N m^{-1}
Registration arm mass, m_r	2.6 kg	Dropper mass including clamps, m_d	0.4 kg
Span length	50 m	Location of the droppers	2.5, 7.5, 12.5, 17.5, 22.5, 27.5, 32.5, 37.5, 42.5, 47.5 m

study are the Korean Honam overhead contact lines, which are a type of simple catenary system. The parameters of the Korean Honam overhead contact lines are given in Table 2.

2.3. Formulation for the contact between a pantograph and a contact wire

A penalty method is used to couple a pantograph and a contact wire. The contact force between a pantograph and a contact wire can be calculated as

$$f_c = k_c \times (y_u - v_c - v_0) \tag{6}$$

where f_c denotes a contact force; k_c denotes a penalty factor, whose value is set to be 50,000 N m^{-1} for a positive contact force and 0 for a negative contact force, as given in EN 50318:2002 [18]; y_u is the dynamic displacement of the pan-head; v_c is the dynamic displacement of a contact wire at a contact point; and v_0 denotes the static equilibrium profile of the contact wire, which was calculated prior to the dynamic simulation. When the contact wire sags, v_0 has a negative value. The vector of nodal forces on a contact wire due to the contact force is given by

$$\hat{\mathbf{f}}_w = f_c\mathbf{N}(\xi) \tag{7}$$

where $\hat{\mathbf{f}}_w$ is the vector of forces to the degrees-of-freedom of the finite element in contact with a moving pantograph, $\mathbf{N}$ represents the vector of the shape function of the Euler–Bernoulli beam element and $\xi = (x_p - L_e(n-1))L_e^{-1}$, x_p is the location of a moving pantograph at time t, L_e is the length of a finite element and n represents the element number in contact.

The coupling between a pantograph and a contact wire can be made by using Eqs. (6) and (7), which give us a coupling stiffness matrix and a coupling force vector for the degrees-of-freedom for both the beam element in contact and the pan-head as

$$\mathbf{K}_{\text{couple}} = k_c\begin{bmatrix} \mathbf{N}(\xi)\mathbf{N}(\xi)^{\mathrm{T}} & -\mathbf{N}(\xi) \\ -\mathbf{N}(\xi)^{\mathrm{T}} & 1 \end{bmatrix} \tag{8}$$

$$\mathbf{f}_{\text{couple}} = \langle\, -k_c v_0(x_p)\mathbf{N}(\xi) \quad k_c v_0(x_p)\,\rangle^{\mathrm{T}} \tag{9}$$

A coupling stiffness matrix and a coupling force vector are added to a global stiffness matrix and a global force vector for the coupling between a pantograph and a contact wire. For a contact wire, the ratio of sag to span is generally 1:1000, or less. For a messenger wire, the ratio is 10:1000, or less. Thus, it is not necessary to consider nonlinear stiffness related to the sag of the wires. However, coupling forces are generated due to the sag of the contact wire, as shown in Eq. (9). For the coupled pantograph–overhead contact lines, the equation

of motion can be written as

$$\mathbf{M}\ddot{\mathbf{v}} + \mathbf{C}\dot{\mathbf{v}} + \mathbf{K}\mathbf{v} = \mathbf{f} \tag{10}$$

where **M**, **C** and **K** are a global mass matrix, a global damping matrix and a global stiffness matrix, respectively, and **f** is the vector of external forces. $\ddot{\mathbf{v}}$, $\dot{\mathbf{v}}$, **v** are the vectors of nodal dynamic displacements, velocities and accelerations, respectively.

2.4. Formulation for a geometrically nonlinear dropper

A dropper serves as a connector between a contact wire and a messenger wire only when it is in tension. When a pantograph passes a dropper, the dropper undergoes a transition from tension to compression, and then returns to tension. A dropper has no resistance to motion if it becomes slack, as when it is in compression. An internal force on a dropper can be computed as

$$f_{\text{drop}} = f_0 + k_d(v_m - v_c) + c_d(\dot{v}_m - \dot{v}_c) \tag{11}$$

where f_{drop} represents an internal force acting on a dropper. v_m and $\dot{v}_m$ represent a dynamic displacement and a velocity of a messenger wire, respectively. v_c and $\dot{v}_c$ represent a dynamic displacement and a velocity of a contact wire, respectively. k_d and c_d represent a stiffness coefficient of a dropper and a damping coefficient of a dropper, respectively. f_0 represents a static force on a dropper due to the dead weight and the pre-sag of a contact wire, which is calculated prior to the dynamic simulation.

At every time step, the slackening of every dropper should be checked. If droppers slacken, that is, $f_{\text{drop}} < 0$, the droppers no longer play a role as connectors between the contact wire and the messenger wire. In this case, the element stiffness matrices and the element damping matrices for the slackened droppers are removed from the global stiffness matrix and the global damping matrix in Eq. (10). Thus, the global stiffness matrix and the global damping matrix are modified as

$$\mathbf{K} = \mathbf{K} - \sum_{j=1}^{\text{ns}} \mathbf{K}_d^j \tag{12}$$

$$\mathbf{C} = \mathbf{C} - \sum_{j=1}^{\text{ns}} \mathbf{C}_d^j \tag{13}$$

where **K** denotes the global stiffness matrix, $\mathbf{K}_d^j$ denotes the element stiffness matrix for the jth slackened dropper, **C** denotes the global damping matrix, $\mathbf{C}_d^j$ denotes the element damping matrix for the jth slackened dropper, and ns is the number of slackened droppers at each time step. In addition, due to the deletion of the element stiffness matrices and the element damping matrices for the slackened droppers, the global force vector in Eq. (10) should be modified as

$$\mathbf{f} = \mathbf{f} - \sum_{j=1}^{\text{ns}} \mathbf{K}_d^j \tilde{\mathbf{v}}_d^j - \sum_{j=1}^{\text{ns}} \mathbf{C}_d^j \tilde{\dot{\mathbf{v}}}_d^j \tag{14}$$

where **f** denotes the global force vector. $\tilde{\mathbf{v}}_d^j = \langle\, \tilde{v}_m \quad \tilde{v}_c \,\rangle^{\mathrm{T}}$ and $\tilde{\dot{\mathbf{v}}}_d^j = \langle \tilde{\dot{v}}_m \quad \tilde{\dot{v}}_c \rangle^{\mathrm{T}}$ are the vectors of dynamic displacements and velocities for the jth slackened dropper, respectively. The dynamic displacements and the velocities in the vectors are the values calculated at the moment of transition from tension to compression.

2.5. Time-integration

Dynamic interaction between a pantograph and a contact wire constitutes a typical wave propagation problem. Thus, proper choice of a time-integration method is important for obtaining accurate solutions and for reducing the computational load. I investigated direct time-integration methods applicable to the pantograph–overhead contact line dynamics. The methods taken into account were the α method proposed by Hilber et al. [19] and the implicit Newmark average–acceleration method [20]. The α method has properties of

numerical damping. The α method is the implicit time-integration method as

$$\mathbf{M}\ddot{\mathbf{v}}_{n+1} + (1+\alpha)\mathbf{C}\dot{\mathbf{v}}_{n+1} - \alpha\mathbf{C}\dot{\mathbf{v}}_n + (1+\alpha)\mathbf{K}\mathbf{v}_{n+1} - \alpha\mathbf{K}\mathbf{v}_n = (1+\alpha)\mathbf{f}_{n+1} - \alpha\mathbf{f}_n \tag{15a}$$

$$\mathbf{v}_{n+1} = \mathbf{v}_n + \Delta t\dot{\mathbf{v}}_n + \frac{\Delta t^2}{2}\left[\frac{1+2\alpha-\alpha^2}{2}\ddot{\mathbf{v}}_n + \frac{(1-\alpha)^2}{2}\ddot{\mathbf{v}}_{n+1}\right] \tag{15b}$$

$$\dot{\mathbf{v}}_{n+1} = \dot{\mathbf{v}}_n + \Delta t\left[\frac{1+2\alpha}{2}\ddot{\mathbf{v}}_n + \frac{1-2\alpha}{2}\ddot{\mathbf{v}}_{n+1}\right] \tag{15c}$$

where subscript n and $n+1$ represent the nth time step and the $(n+1)$th time step, respectively. Δt represents a time step length, and α represents a parameter to control the numerical damping. For stability, α should be in the range of

$$-\tfrac{1}{3} \leqslant \alpha \leqslant 0 \tag{15d}$$

If α is equal to 0, the α method is equivalent to the implicit Newmark average–acceleration method, that is, the trapezoidal rule. The trapezoidal rule has no numerical damping [20].

Both wave propagation and wave reflection substantially affect dynamic interactions between a pantograph and overhead contact lines. Thus, in a pre-tensioned beam, I investigated wave propagation and wave reflection using numerical time-integration methods, by solving two test problems shown in Fig. 3.

The wave propagation speed in the pre-tensioned beam [21] is given by

$$C = \sqrt{\frac{T + \sqrt{T^2 + 16\rho \mathrm{EI}\pi^2 f^2}}{2\rho}} \tag{16}$$

where C is the wave propagation speed, f is an excitation frequency and other variables are given in Fig. 3(a). In the pre-tensioned beam, the wave propagation speed increases as the frequency increases. Thus, high-frequency waves move faster than low-frequency waves.

In order to investigate the characteristics of the wave propagation with both the α method and the trapezoidal method, a step load at $t = 0$ s is applied to the pre-tensioned beam as shown in Fig. 3(a). The analytical solution for the acceleration at the measuring point is available in Ref. [17] as

$$\ddot{y}(x,t) = \sum_{j=1}^{\infty} A_j \omega_j^2 \sin\frac{j\pi L_1}{L}\sin\frac{j\pi x}{L}\cos\omega_j t \tag{17a}$$

where

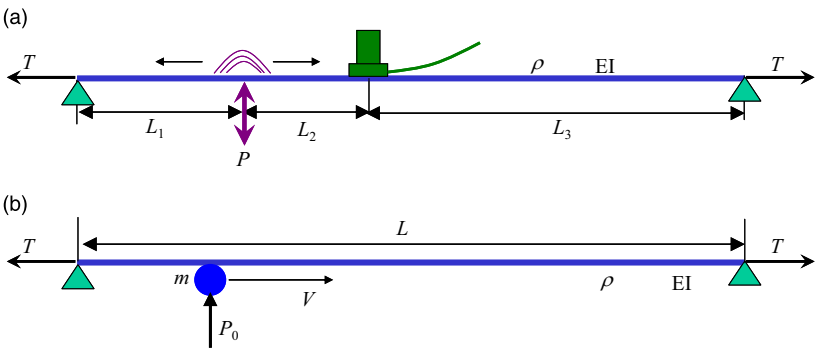

Fig. 3. Definition of the two test problems: (a) wave propagation in the pre-tensioned beam, where $L_1 = 95$ m, $L_2 = 40$ m, $L_3 = 265$ m, $T = 12{,}000$ N, $\rho = 0.987\,\mathrm{kg\,m^{-1}}$ and $\mathrm{EI} = 130\,\mathrm{N\,m^2}$; (b) wave reflection by a moving mass in the pre-tensioned beam, where $L = 50$ m, $P_0 = 50$ N, $m = 3$ kg, $T = 12{,}000$ N, $\rho = 0.987\,\mathrm{kg\,m^{-1}}$, $\mathrm{EI} = 130\,\mathrm{N\,m^2}$ and $V = 198\,\mathrm{km\,h^{-1}}$ or $396\,\mathrm{km\,h^{-1}}$. ● represents the moving mass.

$$A_j = \frac{2P}{L}\frac{1}{\mathrm{EI}(j\pi/L)^4 + T(j\pi/L)^2} \tag{17b}$$

$$\omega_j = \frac{j\pi}{L}\sqrt{\frac{T}{\rho} + \left(\frac{j\pi}{L}\right)^2 \frac{\mathrm{EI}}{\rho}} \tag{17c}$$

P is an excitation force, L is the total length of the pre-tensioned beam in Fig. 3(a), x is the location of a measuring point, j is the mode number, t is the time and other variables are given in Fig. 3(a). Eq. (17) is obtained by using a mode superposition method. Spurious oscillation can be avoided in the mode superposition method, because high-frequency eigenmodes are truncated. I take 650 eigenmodes of the beam to obtain the time history of the accelerations, as shown in Fig. 4(a). The natural frequency for the 650th mode is 101 Hz. Fig. 4(a) shows that high-frequency waves move faster than low-frequency waves.

When it is assumed that a train moves at 200 km h^{-1}, 0.003 s is the time step length that corresponds to the specification of EN 50119:2001 that contact forces between a pantograph and a contact wire shall be simulated for every 0.2 m of the contact wire. But, direct numerical time-integrations with the time step of 0.003 s give us an erroneous time history of the accelerations, as shown in Fig. 4(b), implying that low-frequency waves move faster than high-frequency waves. Both the α method and the trapezoidal method give erroneous results if the time step is 0.003 s.

The time history of the accelerations is given in Fig. 4(c), when the time step for direct numerical time-integrations is equal to 0.001 s. Although both the α method and the trapezoidal method show high-frequency

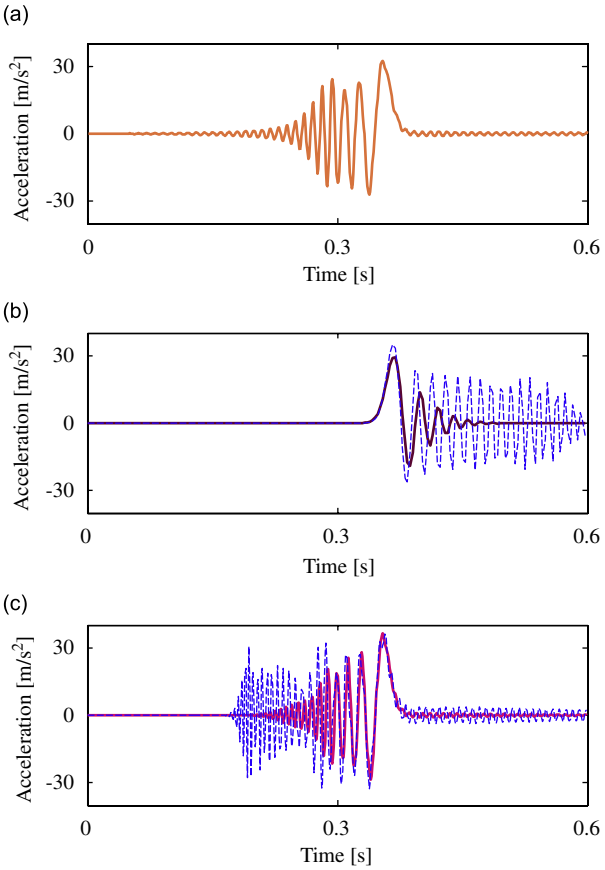

Fig. 4. The effects of numerical time-integration methods on the time histories of accelerations at the measuring point: (a) mode-superposition method, (b) direct time integration with a time step = 0.003 s, (c) direct time integration with a time step = 0.001 s. Solid line in (b) and (c): the α method. Dashed line in (b) and (c): the trapezoidal method.

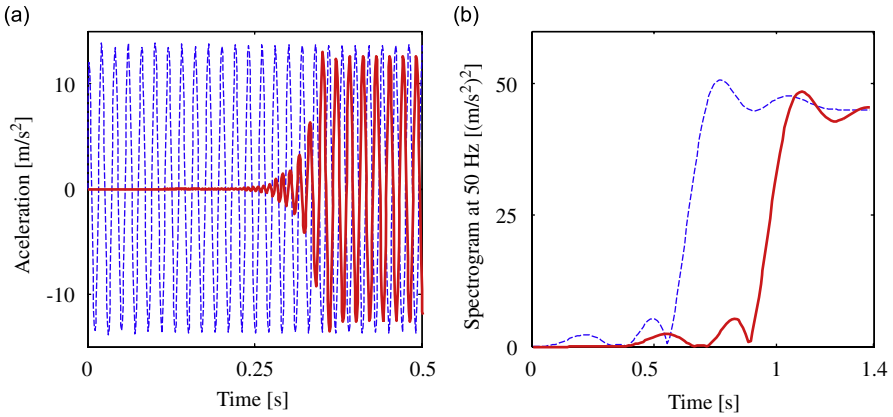

Fig. 5. Extraction of the time difference between the excitation signal and the measured signal in the pre-tensioned beam by using short-time Fourier transformations: (a) time history of accelerations both at the excitation point and at the measuring point when excitation forces $f(t) = 10\sin(100\pi t)$ [N] are given to the pre-tensioned beam and (b) acceleration spectrogram at 50 Hz to locate the time difference between the peaks of the accelerations. Dashed line: at the excitation point. Solid line: at the measuring point.

Table 3
Wave propagation speed in the pre-tensioned beam

Time step length (s)	Excitation frequency (Hz)	Theoretical speed (km h^{-1})	α method		Trapezoidal method	
			Speed (km h^{-1})	Error (%)	Speed (km h^{-1})	Error (%)
0.001	20	111	111	0.0	111	0.0
	50	115	121	5.7	121	5.7
	100	125	143	14.7	148	19.0
0.003	20	111	102	−7.7	102	−7.7
	50	115	95	−17.0	95	−17.0
	100	125	–	–	66	−46.5

waves moving faster than low-frequency waves, the trapezoidal method shows spurious oscillations around the wave front, while the α method does not. In addition, the α method results reasonably correspond to those of the mode superposition method. Thus, it is necessary to set the time step to be 0.001 s or less in order to model the dispersive wave propagation in a contact wire.

In order to investigate the dependency of the wave propagation speed on the frequency in the pre-tensioned beam, sinusoidal forces are given to the pre-tensioned beam, as shown in Fig. 3(a). Three different excitation frequencies are considered: 20, 50 and 100 Hz. A short-time Fourier transformation with a window size of 10 samples is taken for both signals at the excitation point and at the measuring point to obtain the time difference between the two signals. The measuring point is 40 m away from the excitation point. In order to determine the wave propagation speed accurately, band-pass filtering is performed prior to taking the short-time Fourier transformation. The band-pass filtering and the short-time Fourier transformation are performed using a Matlab toolbox [22]. The band-pass filter used was the equi-ripple finite impulse response (FIR) filter. Fig. 5 shows that the time difference between the excitation signal and the measured signal was obtained by using short-time Fourier transformations when excitation forces at 50 Hz were given to the pre-tensioned beam. By applying the same signal-processing procedures, I obtain the wave propagation speeds with different time step lengths and different excitation frequencies, as shown in Table 3. If a time step is equal to 0.001 s, both the α method and the trapezoidal method show that the wave propagation speed gradually increases as the frequency increases. However, the propagation speed has more error at the higher frequencies. The error is more than 10% at 100 Hz, while it is less than 6% at 50 Hz. If the time step is 0.003 s, both the α

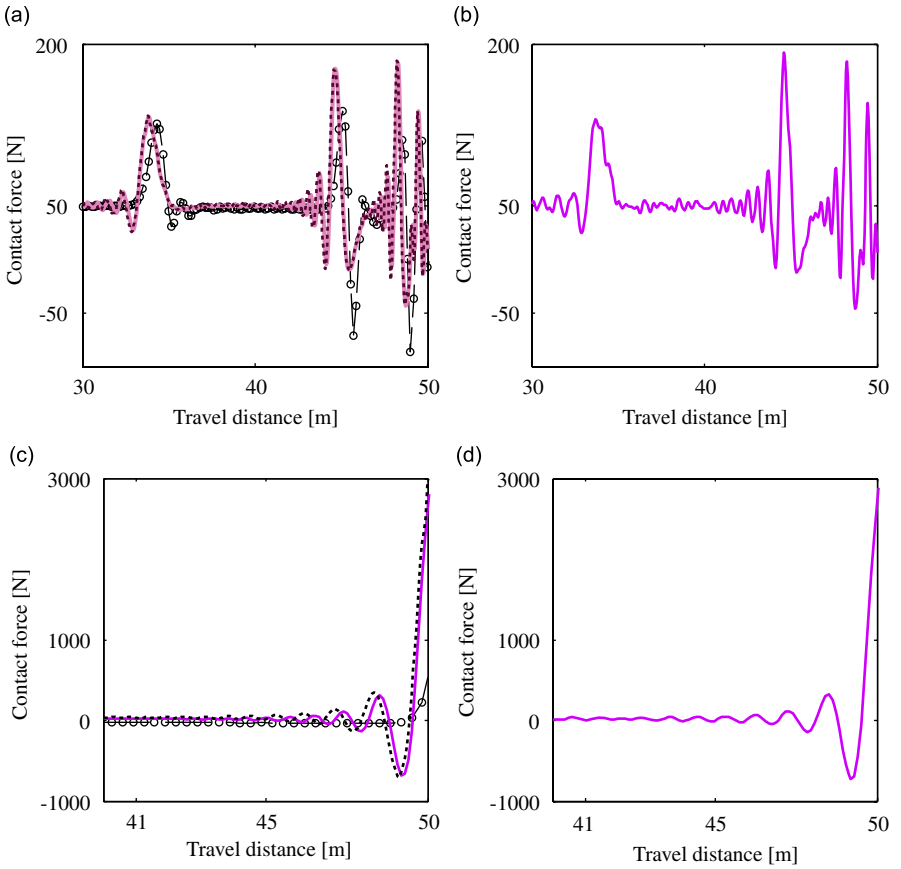

Fig. 6. The effects of a time step length and an element size for the α method on the contact forces between the moving mass and the beam due to the wave reflections at the support: (a) $V = 198\,\mathrm{km\,h^{-1}}$, element size = 0.5 m; (b) $V = 198\,\mathrm{km\,h^{-1}}$, element size = 1 m; (c) $V = 396\,\mathrm{km\,h^{-1}}$, element size = 0.5 m; (d) $V = 396\,\mathrm{km\,h^{-1}}$, element size = 1 m. Solid line: time step = 0.001 s. Dotted line: time step = 0.0005 s. Dashed line with O markers: time step = 0.003 s.

method and the trapezoidal method show that the wave propagation speed decreases as the frequency increases. For the α method, the wave propagation speed cannot be obtained at 100 Hz because the frequency component in the measured signal is too weak. This frequency dependency contradicts the wave propagation in the pre-tensioned beam.

In order to evaluate a convergence condition with the α method, I solve the problem in Fig. 3(b), "wave reflection by a moving mass in the tensioned beam," which is similar to the testing problem presented in Ref. [10]. The parameters of the problem are changed to that of the Korean Honam overhead contact lines. I use the positive penalty factor given by Eq. (6) irrespective of the sign of the contact force. Fig. 6 shows the effects of a time step length and an element size for the α method on the contact forces between the moving mass and the tensioned beam due to the wave reflection at the support. When the speed is $198\,\mathrm{km\,h^{-1}}$, the moving mass meets the reflected wave for the first time at 33.2 m and the peak contact force occurs. This speed is equal to 50% of the wave propagation speed in the pre-tensioned beam at low frequency. The flexural rigidity causes oscillation of the contact force before the peak occurs. The peak causes a new wave to propagate in both directions, to the right and to the left. The wave is reflected at the support. The moving mass meets the reflected wave at 44.3 m. The wave propagation and the wave reflection are repeated as the mass travels to the support. Fig. 6(a) shows that the contact forces with a time step of 0.001 s are almost the same as that with a time step of 0.0005 s, but that the contact forces with a time step of 0.003 s are lower. Thus, convergence is obtained using a time step of 0.001 s if the element size is 0.5 m long. Fig. 6(b) shows that an element size of 1 m causes spurious oscillations, even though the time step is equal to 0.001 s.

Next, I deal with the case in which the speed is 396 km h^{-1}, the wave propagation speed in the pre-tensioned beam. Theoretically, a contact force at the support goes to infinity due to the wave reflection and the Doppler effect [5,23]. Fig. 6(c) shows that a contact force at the support goes up to around 3000 N if the time step is less than or equal to 0.001 s. Considering that the pre-load on the mass is 50 N, the simulated contact force at the support is dramatically increased. However, the contact force is lowered if the time step is 0.003 s. Fig. 6(d) shows that an element size of 1 m causes spurious oscillations, even though the time step is 0.001 s. The lowered contact forces are related to the erroneous characteristics of wave propagation, when the time step is 0.003 s.

In short, the α method ($\alpha = -0.1$) is suited for the pantograph–overhead contact line dynamics, in that the α method is able to reduce spurious oscillations. A converged solution with the α method can be obtained using a time step of 0.001 s if an element is 0.5 m long, irrespective of train speed.

2.6. Dynamic strain

The longitudinal dynamic strain for the large deflection [24] of a contact wire is obtained from

$$\varepsilon_x = -\frac{\partial^2 v}{\partial x^2} y + \frac{1}{2}\left(\frac{\partial v}{\partial x}\right)^2 \tag{18a}$$

where v is the vertical displacement of a wire, x is the longitudinal coordinate, and y is the transverse distance from the neutral axis to the point at which the strain is calculated. The first term on the right-hand side of Eq. (18a) represents the bending strain and the second term represents the nonlinear strain, which is important only for large deflections. Eq. (18a) is often used in technical literature to express nonlinear strain. However, I emphasize that Eq. (18a) is not consistent, because curvature is linearized whereas stretching is nonlinear. The dynamic strain on the upper surface of the contact wire can be numerically obtained using the following equation:

$$\varepsilon_x = -\mathbf{N}^{\mathrm{T}}_{,xx}\mathbf{v}y + \tfrac{1}{2}\mathbf{N}^{\mathrm{T}}_{,x}\mathbf{v}\mathbf{N}^{\mathrm{T}}_{,x}\mathbf{v} \tag{18b}$$

where $\mathbf{v}$ is the solution vector of Eq. (15a) and $\mathbf{N}$ is the vector of the shape function for the Euler–Bernoulli element, $_{,x}$ represents the partial derivative with respect to x, and y is the vertical distance between the upper surface and the neutral axis.

3. Validation

Four FEM models were validated. The first was the pantograph model. The second was the nonlinear dropper model to represent the slackening of a dropper. The third was the overhead contact line model. The fourth was the dynamic interaction between the pantograph and the contact wire. I validated the formulation by comparing the simulated results with the measured values.

3.1. Pantograph model

I will discuss dynamic responses of the overhead contact lines to the Korean tilting pantograph in Section 4. Thus, I validate the dynamic simulation model for the Korean tilting pantograph, as shown in Fig. 2(a). The pantograph is modeled using three levels of the mass–spring–damper. Table 1 shows the definition of the parameters for the simulation model. The pantograph model can be validated by using either the inertance or the receptance. Dynamic characteristics of a pantograph in the low-frequency range are of importance, because excitation frequencies are low. The magnitude of receptance is relatively large in the low-frequency range, while that of inertance is small. Thus, I validate the pantograph model by using the receptance over the frequency range of 1.5–20 Hz. Assuming that $c_u = c_m = 0$ in Fig. 2(a), the receptance of the pantograph, which is defined as the ratio of the displacement of the pan-head to the contact force to the pan-head, can be derived as

$$\frac{y_u}{f_c} = \frac{(k_u + k_m - m_m\omega^2)(k_m + k_l + \mathrm{j}\omega c_l - m_l\omega^2) - k_m^2}{((k_u - m_u\omega^2)(k_u + k_m - m_m\omega^2) - k_u^2)(k_m + k_l + \mathrm{j}\omega c_l - m_l\omega^2) - k_m^2(k_u - m_u\omega^2)} \tag{19}$$

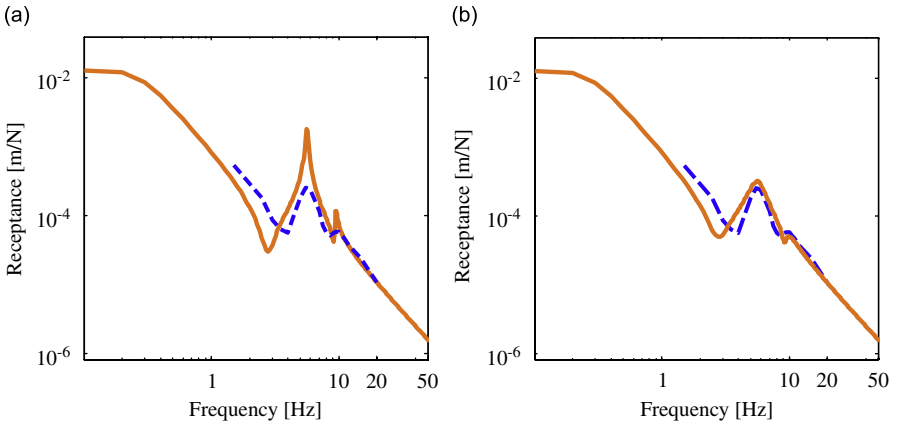

Fig. 7. Receptance of the Korean tilting pantograph: (a) with $c_u = 0\,\mathrm{N\,s\,m^{-1}}$ and (b) with $c_u = 60\,\mathrm{N\,s\,m^{-1}}$. Solid line: simulation model. Dashed line: vibration test.

where y_u represents the displacement of the pan-head, f_c represents the contact force to the pan-head, ω represents the frequency of the harmonic contact force and j represents the imaginary unit. By using Eq. (19) under the assumption that $c_u = c_m = 0$, I obtain the receptance for the Korean tilting pantograph, as shown in Fig. 7(a). The receptance given by Eq. (19) agrees with the receptance from a vibration test [25], except around 5 Hz, as shown in Fig. 7(a). The vibration test was performed at Southwest Jiaotong University in China. The servo-exciting hydraulic system used for the test has a maximum working range of ± 50 mm and a maximum excitation frequency of 50 Hz. The harmonic contact force was given to the center of the pan-head. If it is assumed that $c_u = 60\,\mathrm{N\,s\,m^{-1}}$and $c_m = 0$, the receptance of the pantograph can be obtained numerically instead of using Eq. (19), and agrees well with the receptance from the vibration test, as shown in Fig. 7(b). In addition, Fig. 7 shows that the simulated receptance is constant in the very low-frequency range. Thus, based on the above comparison, the dynamic simulation model can represent the Korean tilting pantograph dynamically, if the frequency of interest is less than or equal to 20 Hz.

3.2. Nonlinear dropper model

The dropper formulations proposed in previous studies have not been validated by measurements taken in the field. To validate the formulation of the geometrically nonlinear dropper, I measured internal forces on a dropper during the passage of a pantograph. As shown in Fig. 8, the dropper nearest the supporting bracket was chosen for the measurement, because that dropper generally undergoes the highest variation in force. I installed a load cell between the contact wire and the dropper, as shown in Fig. 8. The load cell consisted of two non-inductive strain gages (350 Ω) used to form a diagonal bridge for the Wheatstone bridge circuit. One thousand samples per second were taken using a telemetry system to isolate the electricity. Then, low-pass filtering with a cut-off frequency of 50 Hz was performed to remove electrical noise. The type of the low-pass filter used was the equi-ripple FIR filter. The span length of the overhead contact lines was 50 m and the ratio of sag to span was 1:2000. The other parameters of the overhead contact lines are given in Table 2. A pantograph passed the measuring point at a speed of $160\,\mathrm{km\,h^{-1}}$, which corresponded to 40% of the wave propagation speed. Fig. 8 shows that the simulated force agrees well with the measured force. I performed the simulation using a time step of 0.001 s and an element size of 0.5 m. When the pantograph approaches the dropper, the forces acting on the dropper reduce gradually. During the passage of the pantograph, the dropper undergoes slackening for a short period of time. The moment that tension returns, an impulse is applied to the dropper. Afterward, the force damps out slowly. Thus, the comparison confirms that my formulation represents the geometrical nonlinearity of the dropper.

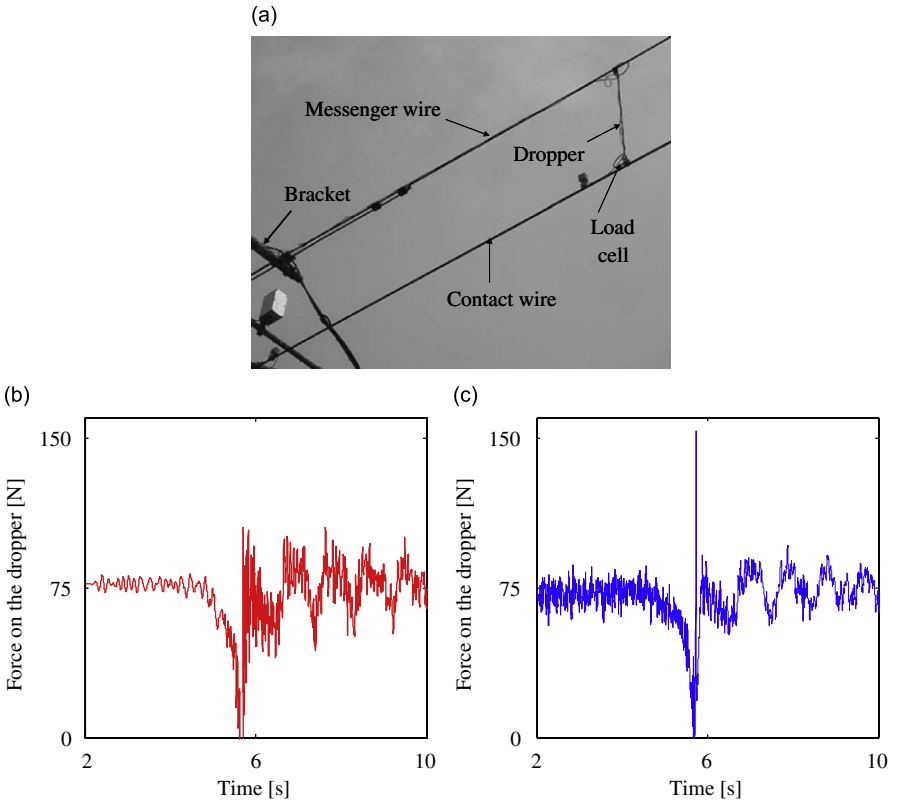

Fig. 8. Comparison of the forces on a dropper for the validation of the nonlinear dropper model: (a) the load cell to measure internal forces in the dropper in Korean Honam line, (b) simulation and (c) measurement.

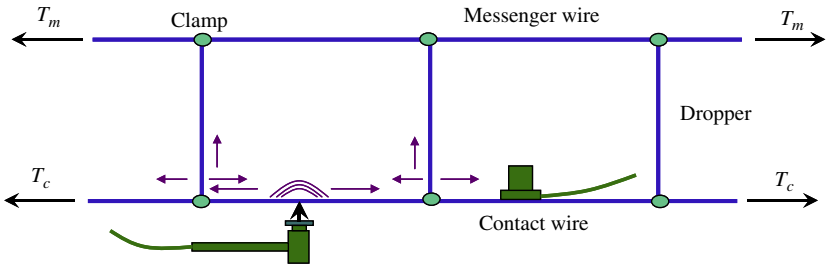

Fig. 9. Wave reflection by droppers in the two levels of overhead contact lines. ⬭ represents the mass summed for one-half of the dropper and its clamp.

3.3. Overhead contact line model

In a contact wire, a disturbance caused by a pantograph propagates in a dispersive manner, that is, the wave propagation speed depends on frequency. This is due to the flexural rigidity of a contact wire. Vibration energy is transferred from a contact wire to a messenger wire through droppers. The vibration of a messenger wire affects the motion of a contact wire inversely. The interaction between a contact wire and a messenger wire through droppers complicates the wave propagation and the wave reflection in the overhead contact lines.

It is important to validate that the overhead contact line model represents the wave reflection by droppers periodically placed in real overhead contact lines. However, in previous work, overhead contact line models have not been validated by using measurements in the field. For this validation, I performed a test with "wave reflection by droppers in two levels of overhead contact lines" as shown in Fig. 9. The parameters in Fig. 9 are

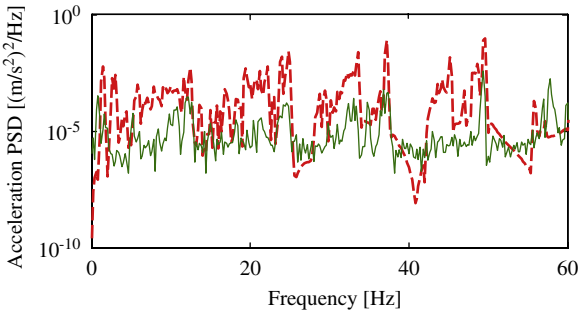

Fig. 10. Comparison of acceleration PSD in the two levels of overhead contact lines for the validation of the overhead contact line model. Solid line: measurement. Dashed line: simulation.

taken from Table 2. A dropper was placed between an excitation point and a measuring point. When an impulse was given to a contact wire, I measured accelerations in the field by using a strain-gage type of accelerometer, which has good dynamic characteristics in low-frequency ranges. The maximum measuring range of the accelerometer is 200 m s^{-2}. Two hundred samples were taken per second. I obtained the power spectral density (PSD) for the measured accelerations by using Welch's method, available in the Matlab toolbox [22], as shown in Fig. 10. The window size for Welch's method was 1024 samples. There are stop bands in the frequency response, which indicates that the reflection of an incident wave happens at the dropper. To compare the stop bands shown in the measurement, I simulated the accelerations using the 2-node Euler–Bernoulli beam elements. Because information on the impulse in the measurement is not available, I assume that 10 N is given to the impact point as an initial condition in the simulation. The power spectral densities for the simulated accelerations are obtained by using the same window size as that applied to the measured data. Fig. 10 shows that the PSD of the simulated accelerations does not agree with that of the measured accelerations, but overall the stop bands in the simulated signal correspond to those in the measured signal up to 40 Hz. Thus, the overhead contact line model is able to approximately represent the stop bands caused by periodically placed droppers up to frequencies higher than 20 Hz, which is the maximum frequency of the validation for a pantograph simulation model.

3.4. Dynamic interaction model to couple a pantograph with a contact wire

Both the vertical displacements and the strains in a contact wire depend on the contact force between the pantograph and the contact wire. Thus, validation of a dynamic interaction model is conducted by comparing simulated results with measured ones with respect to the vertical displacements and the strains in a contact wire.

To validate the accuracy of the simulated vertical displacements in a contact wire, I measured the vertical displacements when a pantograph moved at 160 km h^{-1} under the Korean Honam overhead contact lines. The measurement was performed at the registration arm. A wire sensor was installed between the bracket and the contact wire in order to measure the vertical displacements, as shown in Fig. 11. A full-bridge Wheatstone bridge circuit was used in the wire sensor. The data acquisition for the vertical displacements was performed as mentioned in Section 3.2. The ratio of sag to span of the contact wire in the real overhead contact lines is 1:2000. For comparison with the measured vertical displacements, I simulate the vertical displacements at the registration arm in a contact wire with sag. Fig. 11 shows that the measured vertical displacements and the simulated ones agree well with each other in terms of extreme values and global shape. In Ref. [10], vertical displacements at the registration arm were used to validate a dynamic simulation program. However, the effect of the pre-sag of a contact wire on vertical displacements was not discussed in the previous study. The maximum of vertical displacements at the registration arm is affected by the ratio of sag to span, because the sag forms a force vector given by Eq. (9). If the ratio of sag to span is reduced to 1:20,000, the maximal vertical displacement increases from 3.2 cm to 4.2 cm, as shown in Fig. 11.

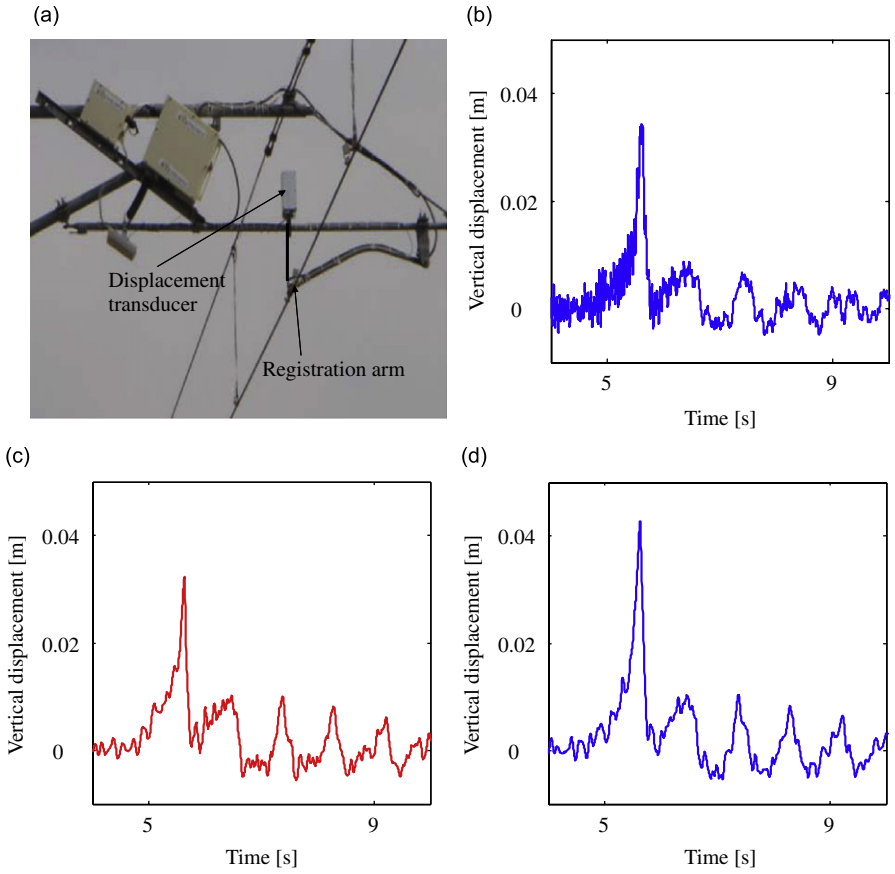

Fig. 11. Comparison of the vertical displacements of the contact wire for the validation of the dynamic interaction between a pantograph and a contact wire: (a) the displacement transducer installed in the Korean Honam line, (b) measured vertical displacements with sag-to-span ratio = 1:2000, (c) simulated vertical displacements with sag-to-span ratio = 1:2000, (d) simulated vertical displacements with sag-to-span ratio = 1:20,000.

My validation is made for vertical displacements in a contact wire with the sag. In addition, both simulated vertical displacements and measured displacements are damped out in a similar manner after the passage of the pantograph. For damping ratios, I chose 0.01 for the contact wire and 0.05 for the messenger wire, based on field experiments [26]. Thus, similar damping of the signals confirms that the damping ratios used in the simulation were reasonable.

Simulated dynamic strains in a contact wire were compared with strains measured when the wire was excited by sinusoidal wave via a cam gear machine [16]. But in the previous studies, the simulated strains were not validated with measurements taken during a pantograph pass. To validate simulated dynamic strains, I measured the dynamic strains in a contact wire at the registration arm in the Korean Metro line during the passage of six pantographs at a speed of 91 km h^{-1}. The speed corresponded to 25% of the wave propagation speed. A non-inductive 350 Ω strain gage was installed on the top of the contact wire. A dummy strain gage was attached to remove electrical noise. A half-bridge was formed for the Wheatstone bridge circuit. The data acquisition for the strain was performed as mentioned in Section 3.2. However, no filtering of the measured data was performed. Fig. 12 shows that the simulated strains agree with the measured strains in terms of maximum values and global shape. Every time the six pantographs pass under the measuring point, sharp peaks in the dynamic strains occur. The width of the peak of the strain is much narrower than that for the vertical displacements. According to Dahlberg [17], a large number of modes in the modal analysis are needed to obtain the converged bending strain in a contact wire. This requires a large amount of computational work. However, my formulation using the penalty method allows us to obtain converged strains if the time step is

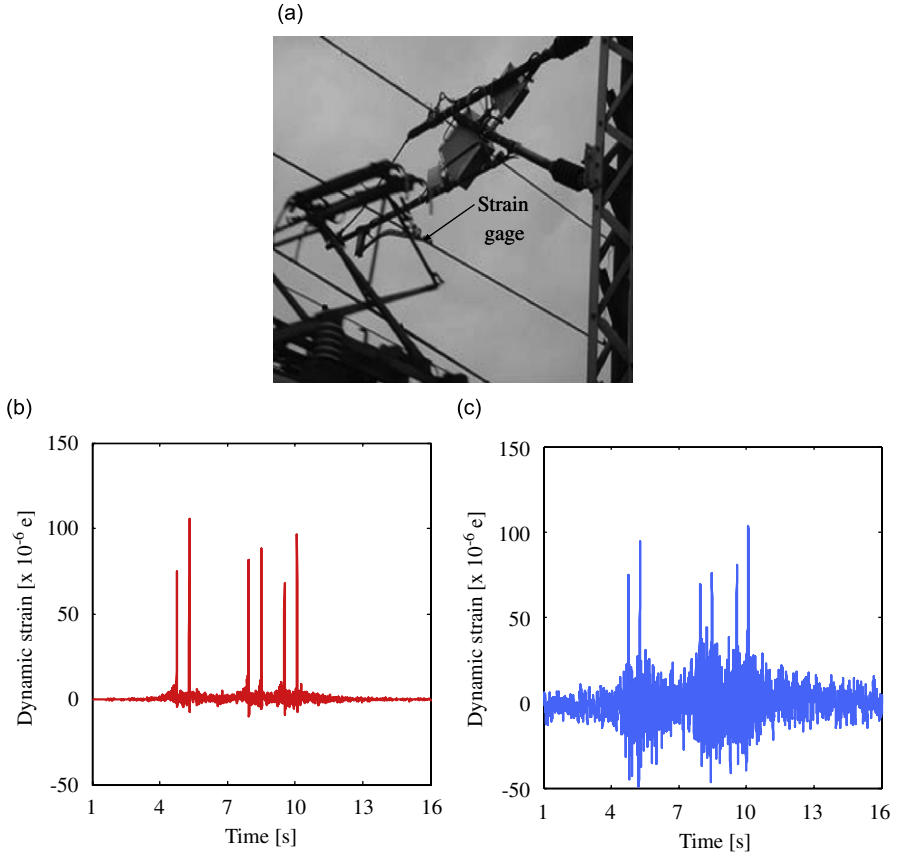

Fig. 12. Comparison of the dynamic strains in a contact wire for the validation of the dynamic interaction between a pantograph and a contact wire: (a) the strain gage on the contact wire of the Korean Metro line, (b) simulated strains and (c) measured strains.

less than or equal to 0.001 s and the element 0.5 m in size. The nonlinear term in Eq. (18a) is negligible in this case. But, the nonlinear term should be taken into account, as a train speed approaches the wave propagation speed.

4. Dynamic responses of overhead contact lines to a moving pantograph

Droppers affect not only the stiffness variation, but also the wave reflection in overhead contact lines. Thus, the dynamic responses of overhead contact lines to a moving pantograph are discussed, relevant to the geometrically nonlinear dropper.

4.1. Variation of contact forces due to uplift force

Generally, a higher input force to a structure causes higher levels of vibration. Intuitively, the increase in uplift force causes higher variation of the contact force between a pantograph and a contact wire. However, the increase in uplift force from 100 to 170 N reduces the variation of the contact forces when the Korean tilting pantograph moves at a speed of 198 km h^{-1} under the Korean Honam overhead contact lines, as shown in Fig. 13(a). The speed is equivalent to 50% of the wave propagation speed. The decrease in the contact force variation is due to the reduction of the stiffness variation along a span. Because of the slackening of the droppers, the stiffness variation is reduced by the increase of the uplift force, as shown in Fig. 14.

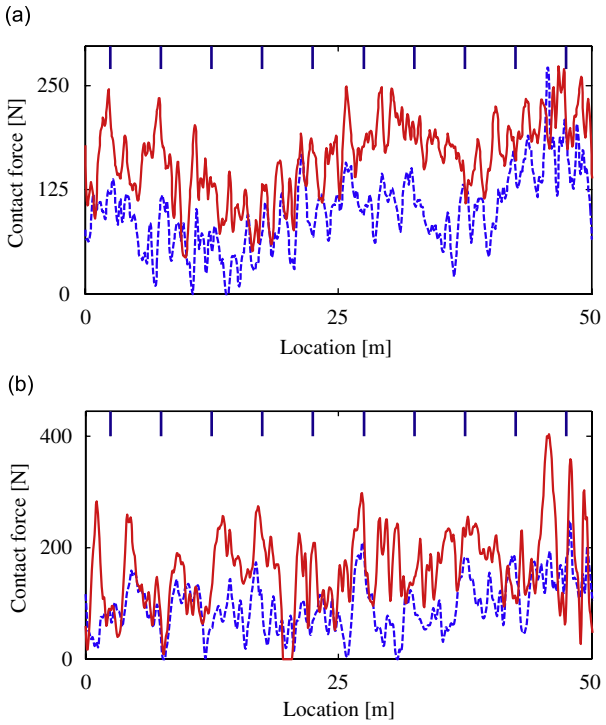

Fig. 13. The effects of uplift forces on the contact forces between a pantograph and a contact wire: (a) train speed = 198 km h^{-1} and (b) train speed = 278 km h^{-1}. Solid line: uplift force = 170 N. Dashed line: uplift force = 100 N.

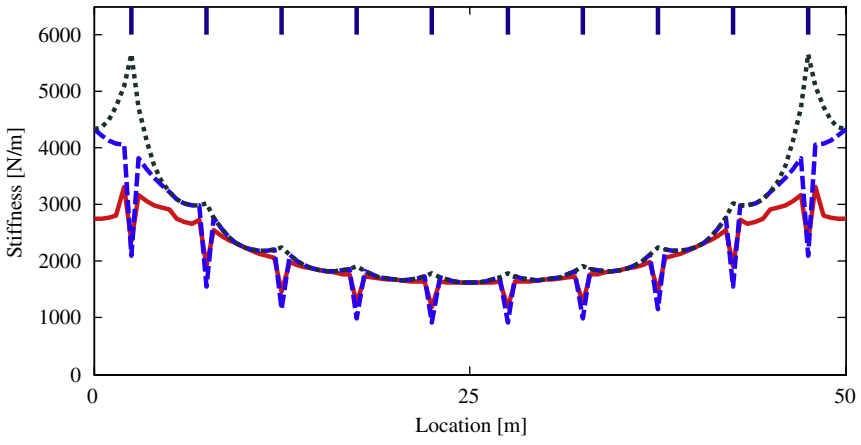

Fig. 14. Stiffness variation along a span for different uplift forces: 170 N (solid line); 100 N (dashed line); 50 N (dotted line).

If the train speed increases to 278 km h^{-1}, that is, 70% of the wave propagation speed, the trend in the contact force variation due to the uplift force is completely changed. Fig. 13(b) shows that the increase of the uplift force from 100 to 170 N causes the larger variation of the contact force. Moreover, the largest peak of the contact force occurs between two neighboring droppers when the uplift force is 170 N. The locations of droppers are indicated by vertical solid lines at the top of Fig. 13(b). The wave reflection creates the loss of contact at high speed, due to the Doppler effect. Moreover, the average stiffness and the stiffness variation of

the overhead contact lines are reduced as the train speed increases [4]. Thus, the increase of the uplift force from 100 to 170 N does not reduce the variation of the contact force when a train moves at a speed of 278 km h^{-1}.

Summing up, the increase of uplift force reduces the variation of the stiffness along a span, because of the slackening of the dropper. Unless the wave reflection becomes a major cause for contact loss, the increase of the uplift force can reduce the variation of the contact force.

4.2. Change in forces acting on the nonlinear dropper

Fatigue failure of the droppers happens in the high-speed line. The change in forces acting on a dropper is a cause for the fatigue. The droppers play a role as wave reflectors in the overhead contact lines, as mentioned in Section 3. Based on Newton's third law, the law of reciprocal actions, I can assume that the wave reflection at the dropper is closely related to the change in forces acting on the dropper.

The wave-reflection coefficient is defined as the ratio of the amplitude of the reflected wave to that of the incident wave. If the stiffness of a dropper is assumed to be infinite, and the damping of a dropper is negligible, the wave reflection coefficient, r, at a dropper [27] is given by

$$r = \frac{-(\mathrm{j}\omega m_{\mathrm{cl}} + 2\sqrt{\rho_m T_m})}{\mathrm{j}\omega m_{\mathrm{cl}} + 2\sqrt{\rho_m T_m} + 2\sqrt{\rho_c T_c}} \tag{20}$$

where m_{cl} represents a dropper clamp mass (kg), and ρ_m and ρ_c represent line densities (kg m^{-1}) for a messenger wire and a contact wire, respectively. T_m and T_c represent tensions (N) for a messenger wire and a contact wire, respectively. j represents an imaginary unit and ω represents a circular frequency (rad s^{-1}). $\sqrt{\rho_m T_m}$ represents impedance for a messenger wire, and $\sqrt{\rho_c T_c}$ represents impedance for a contact wire. Eq. (20) shows that the wave reflection coefficient grows when either the dropper clamp mass or the impedance for the messenger wire is increased.

To investigate the effects of wave reflection parameters on the forces acting on the dropper, I simulate the change in the forces on a dropper next to a bracket, assuming that a pantograph moves at a speed of 220 km h^{-1}. If the mass of a dropper clamp is increased from 0.2 to 1.2 kg, the change in the forces becomes larger, as shown in Fig. 15(a). Moreover, the dropper slackens more frequently. If both the tension and the line density for a messenger wire are increased at the same rate, as shown in Table 4, the impedance for a messenger increases while the wave propagation speed remains constant. In this case, the dropper undergoes a

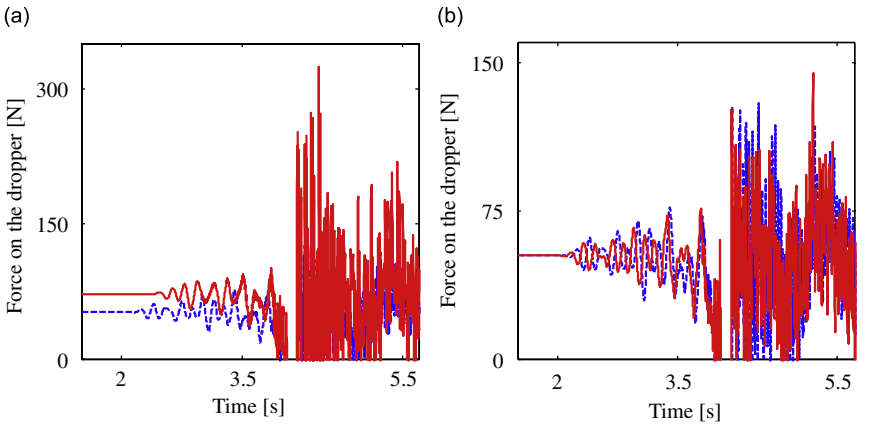

Fig. 15. The effects of wave reflection parameters on the forces acting on the dropper when the train moves at 220 km h^{-1}: (a) different clamp masses, 1.2 kg (solid line) or 0.2 kg (dashed line) and (b) different impedances for the messenger wire, 136.3 (kg N m^{-1})$^{0.5}$ (solid line) or 85.2 (kg N m^{-1})$^{0.5}$ (dashed line).

Table 4
Simulation parameters for different impedances for the messenger wire

Case	Density for messenger wire, ρ_m (kg m^{-1})	Tension for messenger wire, T_m (N)	Wave propagation speed (m s^{-1})	Impedance of messenger wire	Reflection coefficient, r
1	0.605	12,000	141	85.2 (kg N m^{-1})$^{0.5}$	-0.4391 if $m_{cl} = 0$
2	0.968	19,200	141	136.3 (kg N m^{-1})$^{0.5}$	-0.5561 if $m_{cl} = 0$

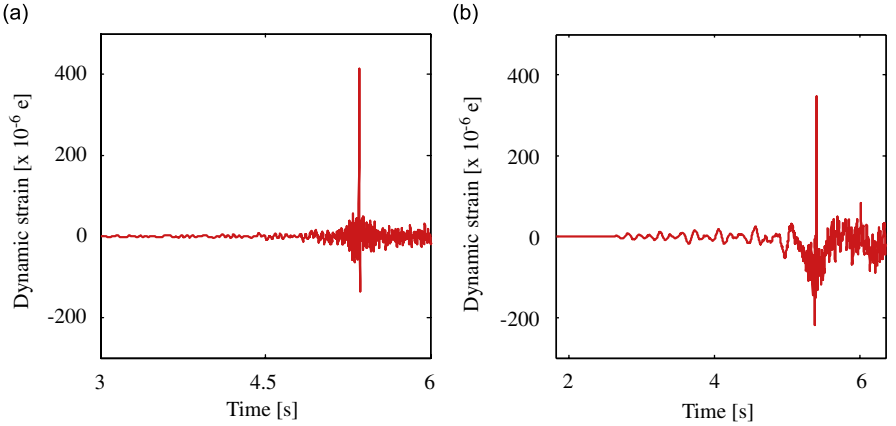

Fig. 16. Dynamic bending strains in a contact wire at different locations when the train moves at 50% of the wave propagation speed: (a) at the middle of neighboring droppers and (b) at the dropper next to the bracket.

larger change in the forces, as shown in Fig. 15(b). Thus, a stronger wave reflection at a dropper causes a larger change in forces acting on a dropper.

4.3. Dynamic strains in a contact wire

Because the droppers are periodically placed, and the contact force is not uniform along a span, the time history of strains in a contact wire depends on the location of the observations. Fig. 16 shows the time history of the strains due to the pantograph's moving at a speed of 198 km h^{-1}. This speed corresponds to 50% of the wave propagation speed in a contact wire. An uplift force of 100 N is applied to the pantograph. Fig. 16(a) shows dynamic strains at the middle of two neighboring droppers. Fluctuating strain acts when the pantograph approaches an observation point. A peak of tensile strain acts at the moment of passage. After the passage, the strain fluctuates again. However, at a dropper next to a bracket, compressive strains appear when the pantograph approaches the dropper, as shown in Fig. 16(b). A peak of tensile strain appears when the pantograph is under the dropper. Afterward, the strains fluctuate again. This phenomenon corresponds to the experimental result [14]. The compressive strains at the dropper are attributed to the fact that an incident wave is reflected at the dropper, and that the reflected wave has the negative phase of the incident wave.

5. Conclusion

Because the slackening of a dropper significantly influences the railway overhead contact line response to a moving pantograph, many authors have proposed formulations to describe slackening, but these have not been validated experimentally. One of the contributions of this paper has been to propose the formulation of a nonlinear dropper and to validate it experimentally. In my formulation, internal forces on a dropper are computed at each time step in order to monitor the slackening of the dropper. Simulated internal forces on the dropper have agreed well with the measured forces in the field. When a pantograph passes a dropper, two

unilateral constraints occur at one point: one is a contact between a pantograph and a contact wire, the other is the slackening of the dropper. In this case, numerical difficulties may arise in pantograph–overhead contact line simulations. But, my formulation does not encounter numerical difficulties, even when a pantograph passes directly under a dropper. In addition, the formulation represents the slackening of the dropper when dissipative effects in a dropper are important.

A wave in a contact wire propagates in a dispersive manner: wave propagation speed increases as frequency increases. A time step of 0.001 s gives us dispersive wave propagation, while a time step of 0.003 s gives us erroneous results when using the α method ($\alpha = -0.1$) or the trapezoidal method for numerical time-integration. The α method with an element size of 0.5 m does not undergo spurious oscillations, whereas the trapezoidal method does. Thus, the α method, with an element size of 0.5 m and a time step of 0.001 s or less, is one of the proper numerical time-integration methods for pantograph–overhead contact line dynamics.

Overhead contact lines have stop-frequency bands in which waves are reflected, because droppers are periodically placed. To validate the overhead contact line model, I measured stop-frequency bands caused by droppers in overhead contact lines. Overall, the stop-frequency bands of overhead contact line models correspond to those of the real overhead contact lines, up to 40 Hz. The maximal vertical displacement at the registration arm is affected by the ratio of sag to span. If the ratio is reduced, the maximum of the vertical displacements at the registration arm increases. Simulated vertical displacements agree well with measured displacements in a contact wire with the sag-to-span ratio of 1:2000. Thus, my simulations represent the effect of the sag on the dynamic response of overhead contact lines. For the thorough validation of pantograph–overhead contact line simulations, the simulated strains in a contact wire were compared with measurements. In previous studies, the simulated strains have not been validated using measurements taken when a pantograph passes. Simulations in this study agreed with the measurements in terms of maximum values and global shape.

Conclusively, my validated spatial finite element approach combined with the numerical time-integration method can be used to accurately analyze the dynamic responses of the overhead contact lines to a moving pantograph.

Acknowledgments

This work has been improved by the advice of Professor Yoon Young Kim in Seoul National University, Korea. This advice is gratefully acknowledged. The author would also like to thank the referees for their valuable comments. This work was supported by a research grant from the Korean Government.

References

[1] G. Gilbert, H.E.H. Davies, Pantograph motion on a nearly uniform railway overhead line, *Proceedings of the IEE* 113 (3) (1966) 485–492.

[2] J.R. Ockendon, A.B. Tayler, The dynamics of a current collection system for an electric locomotive, *Proceedings of the Royal Society of London A* 322 (1971) 447–468.

[3] G. Poetsch, J. Evans, R. Meisinger, W. Kortüm, W. Baldauf, A. Veitl, J. Wallaschek, Pantograph/catenary dynamics and control, *Vehicle System Dynamics* 28 (1997) 159–195.

[4] T.X. Wu, M.J. Brennan, Dynamic stiffness of a railway overhead wire system and its effect on pantograph–catenary system dynamics, *Journal of Sound and Vibration* 219 (3) (1999) 483–502.

[5] A.V. Metrikine, A.L. Bosch, Dynamic response of a two-level catenary to a moving load, *Journal of Sound and Vibration* 292 (2006) 676–693.

[6] T. Park, C. Han, J. Jang, Dynamic sensitivity analysis of the pantograph of a high-speed rail vehicle, *Journal of Sound and Vibration* 266 (2003) 235–260.

[7] J. Kim, H. Chae, B. Park, S. Lee, C. Han, J. Jang, State sensitivity analysis of the pantograph system for a high-speed rail vehicle considering span length and static uplift force, *Journal of Sound and Vibration* 303 (2007) 405–427.

[8] O. Lopez-Garcia, A. Carnicero, J.L. Maroño, Influence of stiffness and contact modeling on catenary–pantograph system dynamics, *Journal of Sound and Vibration* 299 (2007) 806–821.

[9] C.N. Jensen, H. True, Dynamics of an electric overhead line system and moving pantographs, *Vehicle System Dynamics* 28 (Suppl.) (1998) 104–113.

[10] A. Collina, S. Bruni, Numerical simulation of pantograph–overhead equipment interaction, *Vehicle System Dynamics* 38 (4) (2002) 261–291.
[11] J. Seo, S. Kim, I. Jung, T. Park, J. Mok, Y. Kim, J. Chai, Dynamic analysis of a pantograph–catenary system using absolute nodal coordinates, *Vehicle System Dynamics* 44 (8) (2006) 615–630.
[12] J.P. Massat, J.P. Laine, A. Bobillot, Pantograph–catenary simulation, *Vehicle System Dynamics* 44 (Suppl.) (2006) 551–559.
[13] G. Galeotti, P. Toni, Overhead contact line elasticity optimization for railway high speed running, *Computers and Structures* 65 (6) (1997) 975–983.
[14] K. Manabe, High-speed contact performance of a catenary–pantograph system (an experimental study using a dynamically scaled model), *JSME International Journal Series III* 32 (2) (1989) 200–205.
[15] European Committee for Electrotechnical Standardization EN 50119:2001, *Railway applications—fixed installations—electric traction overhead contact lines*, 2001.
[16] W. Zhang, Y. Liu, G. Mei, Evaluation of the coupled dynamical response of a pantograph–catenary system: contact force and stresses, *Vehicle System Dynamics* 44 (8) (2006) 645–658.
[17] T. Dahlberg, Moving force on an axially loaded beam with applications to a railway overhead contact wire, *Vehicle System Dynamics* 44 (8) (2006) 631–644.
[18] European Committee for Electrotechnical Standardization EN 50318:2002, *Railway applications—current collection systems—current collection systems validation of simulation of the dynamic interaction between pantograph and overhead contact line*, 2002.
[19] H.M. Hilber, T.J.R. Hughes, R.L. Taylor, Improved numerical dissipation for time integration algorithms in structural dynamics, *Earthquake Engineering and Structural Dynamics* 5 (3) (1977) 283–292.
[20] R.D. Cook, D.S. Malkus, M.E. Plesha, *Concepts and Applications of Finite Element Analysis*, third ed., Wiley, New York, 1989.
[21] S.Y. Park, B.U. Jeon, J.M. Lee, Y.H. Cho, Measurement of low-frequency wave propagation in a railway contact wire with dispersive characteristics using wavelet transform, *Key Engineering Materials* 321–323 (2006) 1609–1615.
[22] *Matlab User's Guide for Signal Processing Toolbox 6*, Mathworks, 2007.
[23] F. Kießling, R. Puschmann, A. Schmieder, *Contact lines for electric railways planning, design and implementation*, Publicis, 2001.
[24] J.S. Przemieniecki, *Theory of Matrix Structural Analysis*, McGraw-Hill Book Company, New York, 1968.
[25] T. Ko, G.N. Kim, S.H. Han, Y.M. Choi, The test for following characteristics of pantograph on TTX, *Spring Conference of Korean Society for Railway* (2006) 15–20.
[26] Y.H. Cho, J.M. Lee, S.Y. Park, E. Lee, Robust measurement of damping ratios of a railway contact wire using wavelet transforms, *Key Engineering Materials* 321–323 (2006) 1629–1635.
[27] M. Aboshi, Influence of wave motion of contact wire on contact force fluctuation (2nd report, experiments in practical catenary–pantograph system), *JSME Journal Series C* 64 (622) (1998) 30–37.